Chapter 4

Thermo-optical correlation for room temperature synthesis: cold-sintered lead halides

Publication: ***Manish Kumar***, *Vani Pawar, Priyanka A. Jha, S.K. Gupta, A.S.K. Sinha, Pardeep K. Jha, and Prabhakar Singh, Journal of Materials Science: Materials in Electronics, 30, 6, 6071-6081 (2019).*

CHAPTER 4: Thermo-Optical Correlation for Room Temperature Synthesis: Cold Sintered Lead Halides

4.1 Introduction

It has been discussed in chapter 3 that $CsPbI_3$ and $CsPbBr_3$ compounds are more stable than that of $CsPbBr_xI_{3-x}$ (x= 0.5 to 2.5, in the step size of 0.5) compounds. This chapter is divided into two parts: in part A, the formation of $CsPbI_3$ and $CsPbBr_3$ through cold sintering synthesis has been analyzed using thermo-dynamical parameters ΔG and ΔS. The thermodynamical stability using ΔS is also discussed. For further verification of the formation of these compounds, structural and optical properties are studied. A thermo-optical correlation between free energy and band gap is also established for the two Perovskites halides. The results obtained in the present chapter work are compared (on the basis of synthesis technique) with the existing literature. Further, in part B, we were synthesized the polycrystalline bulk compound of $CsPbI_3$ by the cold sintering via solid-state reaction (SSR) method. Before understanding the charge carrier dynamics reported in this chapter, it is studied the thermo-optical correlation, structural, morphological, current-voltage curve, and optical properties that have been discussed in part A. In addition, the degradation in the current–voltage curve was observed when exposed to AM 1.5G sunlight. Therefore, to understand the degradation behavior in the current–voltage curve, we have focused on the investigation of the charge transport mechanism through the material. we studied the hopping conduction, and relaxation mechanisms with temperature. For this, electrical properties are characterized by the real and imaginary part of the permittivity, modulus, and ac conductivity within the frequency range 10 to 10^6 Hz for different temperatures between room temperature to 153 °C.

4.2 Experimental Procedure

$CsPbBr_3$ and $CsPbI_3$ were prepared by the solid-state reaction method at room temperature. For preparing $CsPbBr_3$ and $CsPbI_3$, the powders of CsX (X = I, 99.9 % and Br 99.999 %, Aldrich) and $PbBr_2$ (98 %, Aldrich) were weighed in stoichiometric quantities. The powder of CsX (X = I, Br) and PbX_2 (X = I, Br) were mixed (Humidity, 34 %) and ground up to 2 hours in pestle mortar at room temperature in air. After grinding, the powders of $CsPbBr_3$ and $CsPbI_3$ were pelletized using hydraulic press and finally sintered in the vacuum oven at 80 °C for 1 hour.

The thermodynamics of the powders obtained has been studied using SHIMADZU DSC-60 plus 230V. The resulting perovskite products were characterized by X-ray diffraction technique (XRD) using Rigaku Miniflex for the identification of phase formation. The diffraction patterns were refined by Rietveld refinement method using FULLPROF suite software. The Raman spectra of perovskite powders were detected by DXRxi Raman imaging microscope by Thermo SCIENTIFIC with the excitation wavelength of 780 nm. The optical absorption spectrum was measured by JASCO V-770 ultraviolet-visible (UV) spectrometer. The X-ray photoelectron spectroscopy (XPS) spectrum was recorded at KRATOS (Amicus model) high performance analytical instrument utilizing Mg target under 10^{-6} Pa pressure. I-V curve measurement has been performed using Keithley 2450 source meter on exposure to radiation through Science tech solar simulator class: AAA with AM1.5 G filter and higher collimated beam. Further, the impedance measurement of the studied perovskite material was done using Solartron 1260 A impedance analyzer at 1V.

Synthesis of the $CsPbX_3$ (X = I and Br) and Analysis of the Results

4.3 Results and Discussion

4.3.1 Thermodynamics

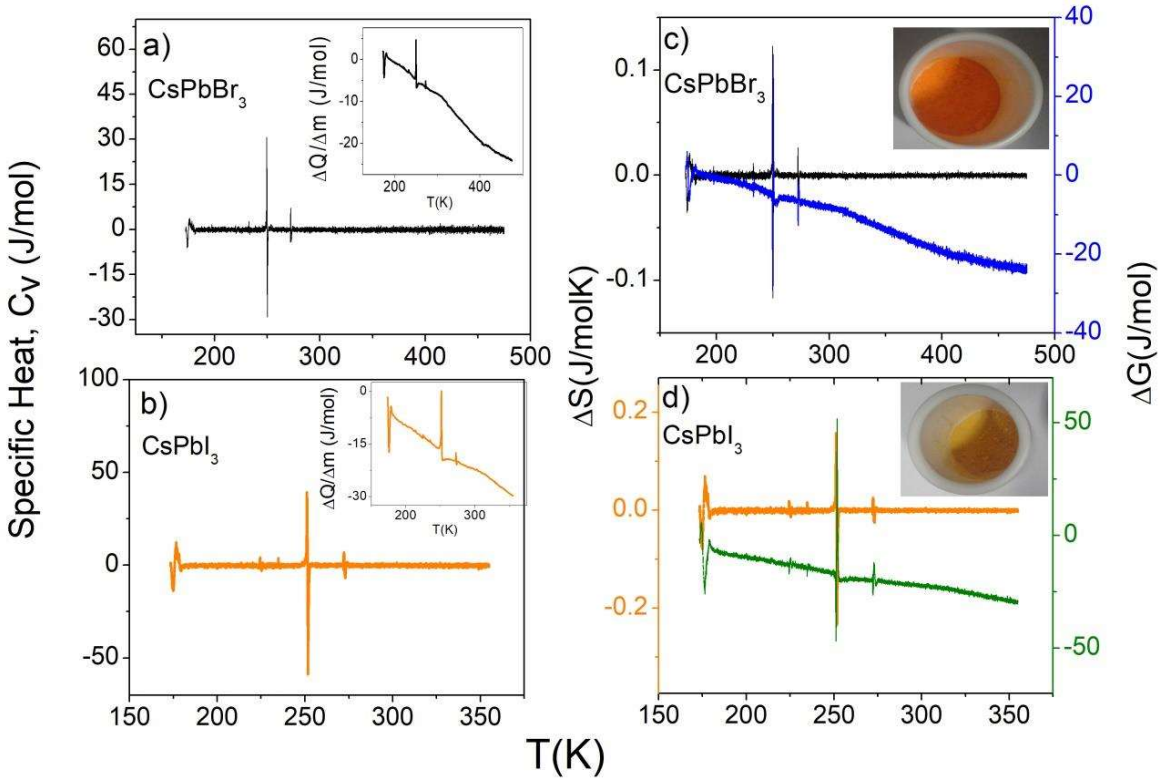

Figure 4.1: (a, b) Variation of specific heat *(C_V)* (insets show variation of (ΔQ/Δm)) and (c, d) Variation of change in Gibbs free energy (ΔG) and entropy (ΔS) with temperature for $CsPbBr_3$ and $CsPbI_3$, respectively.

Figure 4.1(a, b) shows the variation of specific heat (C_V) with temperature for $CsPbBr_3$ and $CsPbI_3$, respectively. From the specific heat graphs, it is observed that in $CsPbBr_3$ and $CsPbI_3$, there are three peaks at ~ 177 K, 252 K and 272 K. The heat loss graphs (shown in inset) depict two peaks in $CsPbBr_3$: one endothermic peak at 175 K and one exothermic peak at 249 K. Similarly, one exothermic large peak is observed in $CsPbI_3$ at ~252 K showing that

the crystallization of these samples is completed well below room temperature, indicating that room temperature would be the higher temperature for the conversion from amorphous to crystalline substances. Moreover, some small exothermic peaks are also observed e.g. at ~275 K in both the compounds apart from major variation at ~250 K. The specific heat at 250 K is observed to be higher in $CsPbI_3$ (37 J/mol) than $CsPbBr_3$ (29 J/mol). Fig. 4.1(c and d) shows the variation of ΔG and ΔS with temperature. In $CsPbBr_3$, value of ΔG is -27 J/mol and ΔS is 0.122 J/mol K, whereas, in $CsPbI_3$, value of ΔG is -40J/mol and ΔS is 0.159 J/mol K at 252 K. The higher negative values of ΔG and higher positive values of ΔS favor the product formation well below room temperature more in $CsPbI_3$. In addition to it, there is gradual increase in ΔG for $CsPbI_3$ and $CsPbBr_3$, showing the possibility of forward reaction. In $CsPbBr_3$, the increase in ΔG is steeper than that of in $CsPbI_3$, whereas, entropy is nearly constant showing the thermodynamical stability of the studied samples.

4.3.2 X-ray diffraction

The phase formation of $CsPbBr_3$ and $CsPbI_3$ was verified by X-ray diffraction with Cu-Kα radiation (λ = 1.540598 Å) in 2θ range of 5^o to 70^o with a step size of 0.01^o at room temperature. Figure 4.2 shows the XRD patterns of $CsPbBr_3$ and $CsPbI_3$ samples. It is observed that, X-ray diffraction of $CsPbBr_3$ and $CsPbI_3$ show the orthorhombic phase with P*nma* symmetry. The comparison of X-ray diffraction patterns shows that $CsPbI_3$ has more diffraction peaks than that of $CsPbBr_3$. The diffraction peak (121) corresponding to $2\theta \approx 21.53^o$ of $CsPbBr_3$ is shifted to lower angle in comparison to the diffraction peak (212) of $CsPbI_3$ corresponding to $2\theta \approx 27.02^o$ (as highlighted in Fig. 4.2 in gray rectangle). It may be attributed to the lattice contraction as I^- (ionic radius 2.2 Å) is larger than Br^- (ionic radius 1.96 Å). This should create more disorder in $CsPbI_3$ sample.

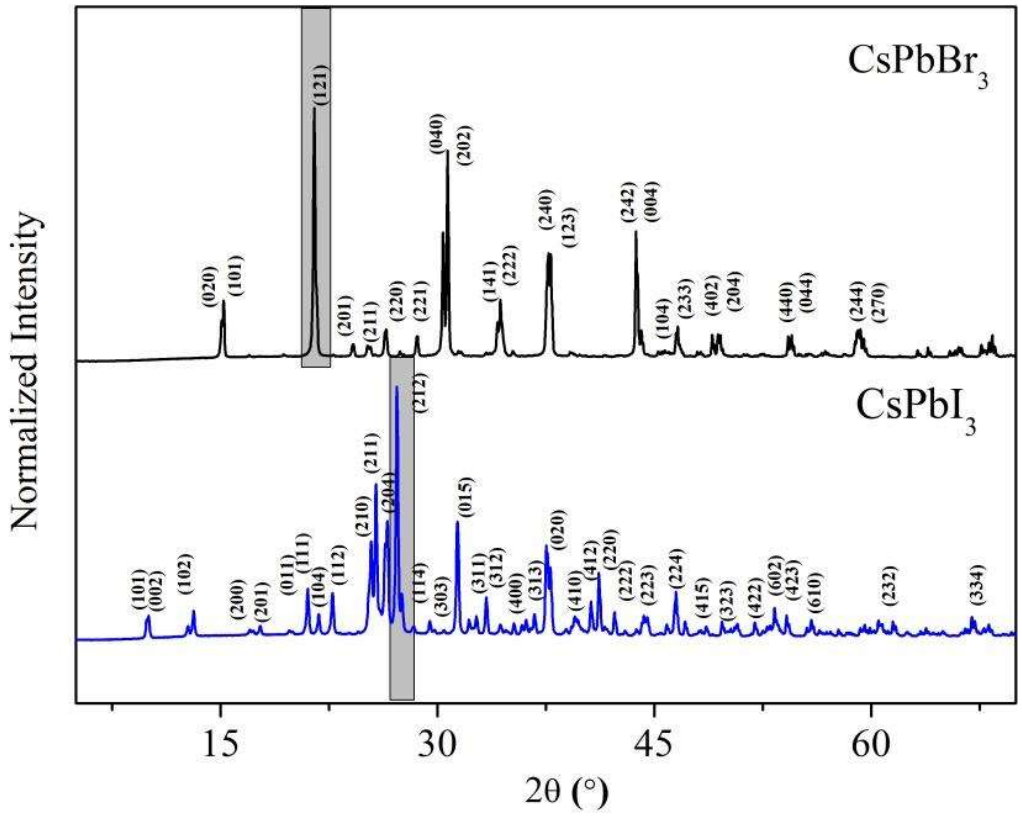

Figure 4.2: Room temperature indexed X-ray diffractograms showing the single phase formation for $CsPbBr_3$ and $CsPbI_3$, respectively. Most intense peak is highlighted in gray rectangle to show change in the XRD pattern with replacement of Br with I.

For the strain in the lattice, microstrain and crystallite size have been calculated using Williamson-Hall (W-H) equation (graphs not shown here).

$$\beta cos\theta = 0.9\frac{\lambda}{t} + 4\varepsilon sin\theta \qquad (4.1)$$

where β, λ, ε and θ are the full width at half maximum (FWHM) of the diffraction peak, the x-ray wavelength (λ= 1.54098 Å), microstrain and Bragg angle of the diffraction peak, respectively. It is observed that the lattice of $CsPbI_3$ ($\in$ = 0.09) is more strained than that of $CsPbBr_3$ ($\in$ = 0.03). The average crystallite sizes of $CsPbBr_3$ and $CsPbI_3$ materials obtained from W-H plots are 102.58 nm and 60.50 nm, respectively. For further verification of phase formation, the XRD of these materials are well refined with P*nma* symmetry using

FULLPROF software package and the lattice parameters, R_{exp}, R_p and R_{wp} etc. obtained after refinement are mentioned in Table 4.1.

Table 4.1: Lattice parameters and fitting parameters for the studied samples.

Parameters	**$CsPbBr_3$**	**$CsPbI_3$**
Structure	Orthorhombic	Orthorhombic
Space group	P*nma* (62)	P*nma* (62)
Lattice parameters	$\alpha=\beta=\gamma=90°$	$\alpha=\beta=\gamma=90°$
a (Å)	8.261559	10.471622
b (Å)	11.766452	4.804939
c (Å)	8.212267	17.798300
Cell volume ($Å^3$)	798.3081	895.5330
R_{exp}	2.79	2.71
R_p	6.54	8.99
R_{wp}	6.85	11.4
RF-factor	2.74	2.88
Bragg R-factor	3.85	3.37

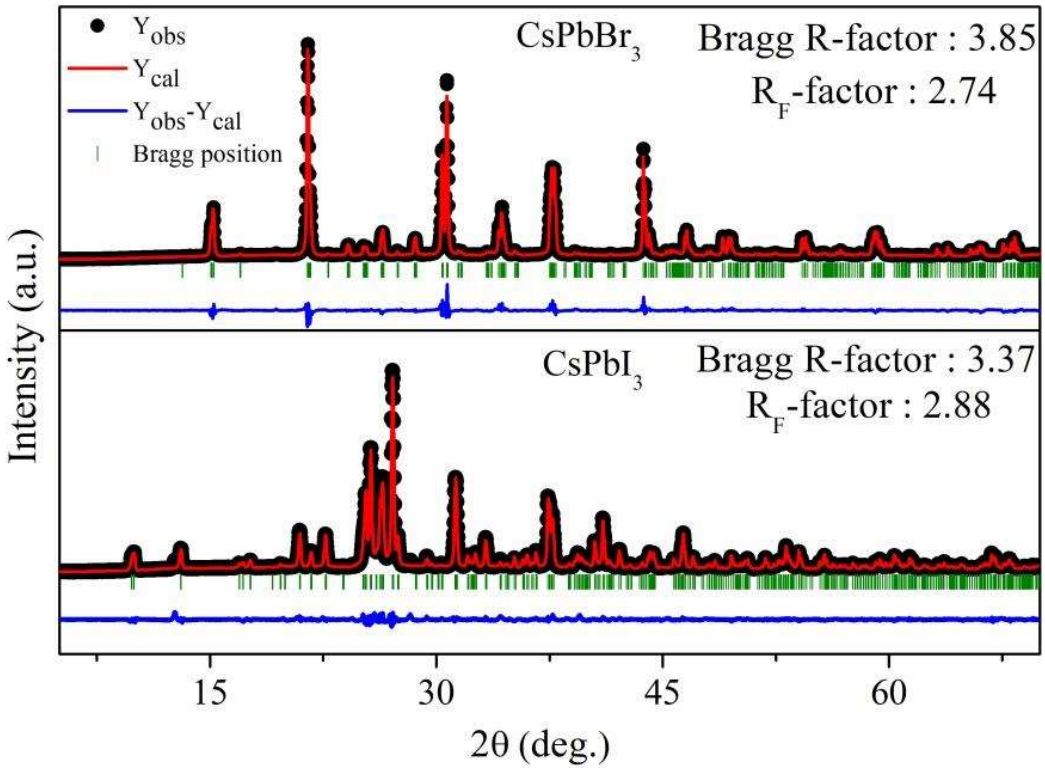

Figure 4.3: Rietveld refinement of XRD with the evaluated parameters for $CsPbBr_3$ and $CsPbI_3$, respectively.

4.3.3 Raman Spectroscopy

In order to understand the structure of these samples in depth, Raman measurements were carried out in the wave number range 50 cm^{-1} to 500 cm^{-1}. The Raman spectra of $CsPbBr_3$ and $CsPbI_3$ were obtained by exciting 780 nm lasers light at the room temperature (Fig. 4.4). According to Bilbao Crystallographic server, the number of modes for P*nma* symmetry should be 9. On deconvoluting the data, we have observed that number of modes in $CsPbI_3$ (9) is more than that in $CsPbBr_3$ (7). But the number of modes is less than 9 inferring the presence of same symmetry. The difference in number of modes in Raman and number of peaks in XRD are very well correlated. For the number of peaks in XRD pattern, we studied $h^2+K^2+l^2$; there are nearly double reflections observed along the c-axis in the $CsPbI_3$ in comparison to the b- axis

orientation in $CsPbBr_3$. This shows the different orientation of the two compounds. In case of P*nma* symmetry, the modes observed are A_g, B_{1g}, B_{2g} and B_{3g} stretching modes. The A_g and B_g modes correspond to the stretching of Pb - I and Cs - I bonds. The intensity of stretching mode observed at ~ 110 cm^{-1} is higher in $CsPbI_3$ than that of $CsPbBr_3$. In addition to it, the FWHM observed for the band corresponding to ~ 110 cm^{-1} is less in $CsPbI_3$ (19.70 cm^{-1}) than $CsPbBr_3$ (33.42 cm^{-1}). This shows that bonds are more stretched in $CsPbI_3$ in comparison to $CsPbBr_3$.

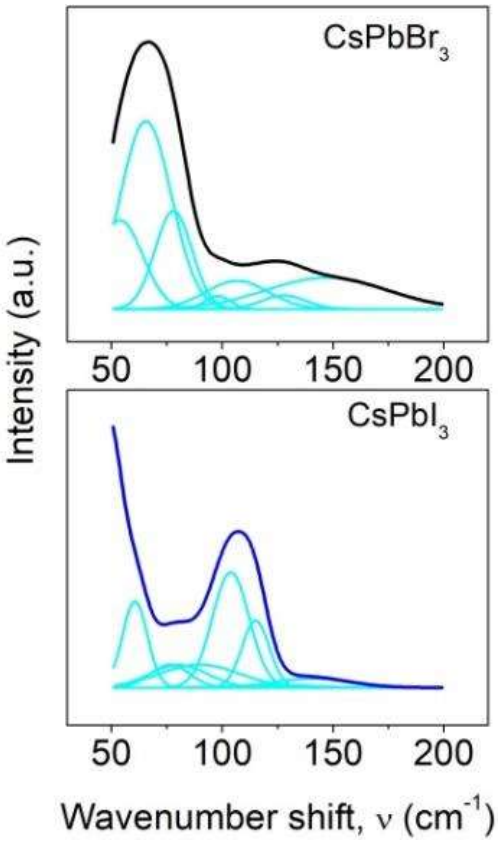

Figure 4.4: De- convoluted Raman spectra of $CsPbBr_3$ and $CsPbI_3$ showing the number of modes in agreement with the Pnma symmetry according to Bilbao crystallographic server.

4.3.4 Microstructural Studies

To study the grain morphology and density of the studied samples, SEM micrographs of $CsPbBr_3$ and $CsPbI_3$ are recorded and shown in Fig. 4.5. It is observed that $CsPbBr_3$ show a large distribution of grains in spherical form with pores. But in case of $CsPbI_3$, the distribution of grains is in the regular form without voids. It is found through grain size distribution histograms (Fig. 4.5 respective insets) that the average grain sizes of $CsPbBr_3$ and $CsPbI_3$ are 1.90 μm and 0.51 μm, respectively and can be correlated with the crystallite size as larger crystallites result larger grains in case of $CsPbBr_3$.

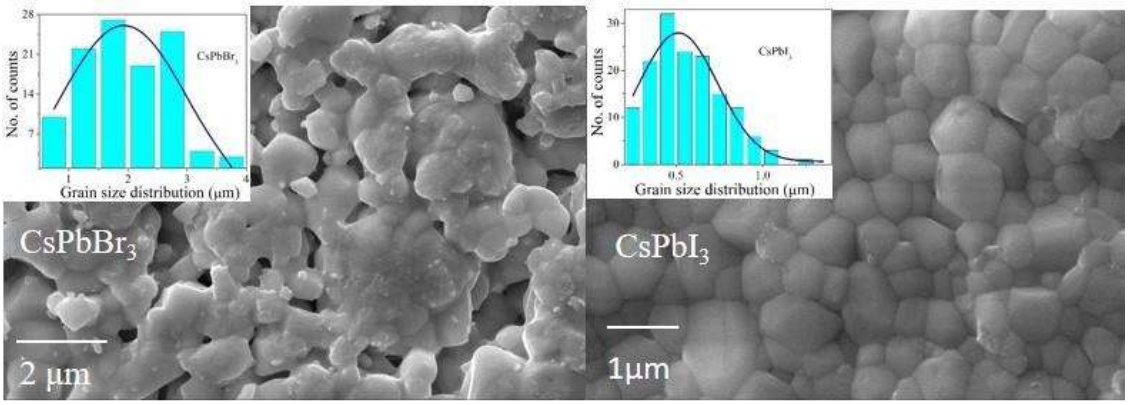

Figure 4.5: SEM micrographs of $CsPbBr_3$ and $CsPbI_3$ samples.

4.3.5 X-ray Photoelectron Spectroscopy (XPS) studies

The XPS spectra of $CsPbBr_3$ and $CsPbI_3$ were analyzed for the constituent's elemental details after calibration with the C 1s peak at 284.5 eV. Figure 4.6 shows the wide range spectrum to confirm the oxidation state of different ions. All peaks are assigned from the National Institute of Standard and technology (NIST) XPS database [149]. To confirm the presence of Cs, Pb, I and Br in the powder samples, The most intense photoelectric peaks are observed for Cs $3d_{5/2}$, Cs $3d_{3/2}$, Cs $4d_{3/2}$, Pb $4f_{5/2}$, I $3d_{5/2}$ and Br $3d_{5/2}$. Other low intensity peaks

are collected for Cs $4p_{3/2}$, Cs $3p_{3/2}$, C 1s, Br $3p_{1/2}$ and Br $3s_{1/2}$. Further, some Auger peaks – Cs Auger and Cs loss are also observed. The presence of constituent elements has been confirmed in the XPS spectrum of these materials.

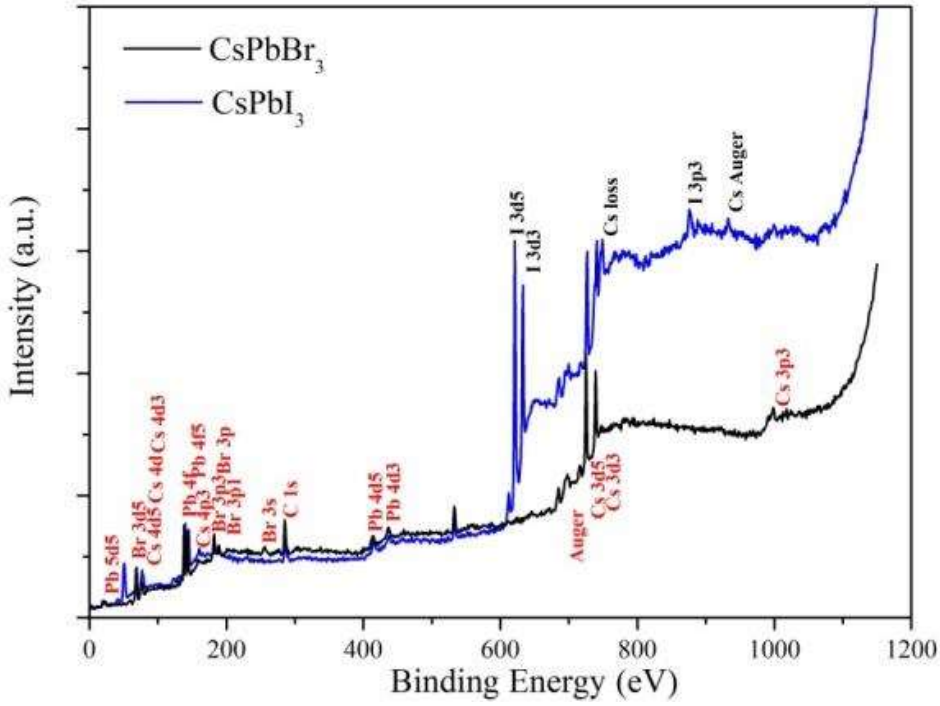

Figure 4.6: Wide range XPS spectrum for the confirmation of oxidation states of different ions.

Figure 4.7 shows the deconvoluted comparative elemental XPS spectrum along with the spin orbit interaction. The presence of $3d_{5/2}$ and $3d_{3/2}$ for Cs, $4f_{5/2}$ and $4f_{3/2}$ for Pb and doublets $3d_{5/2}$ and $3d_{3/2}$ for I^- and Br^- confirms the electronic states. After analyzing the data, a left chemical shift of Cs peaks is observed for $CsPbBr_3$ showing the change in oxidation state of Cs. It is also observed that in the peak corresponding to Cs, there is a formation of hump in $CsPbI_3$ and can be classified as auger peak. In addition to it, Pb doublets of $4f_{5/2}$ and $4f_{3/2}$ peaks are observed along with the satellite features. In Br^- and I^- spectra, some shake ups are observed leading to the formation of some small peaks [151]. The change in oxidation state indicates the

higher binding energy of I^- than that of Br^-. The satellite features observed in Pb indicate the metal – ligand interaction i.e. interaction between Pb and X (= I, Br). Also, the intensity of doublets is swapped in I and Br i.e. the peak having higher intensity in $CsPbBr_3$ has lower intensity in $CsPbI_3$ or vice-versa.

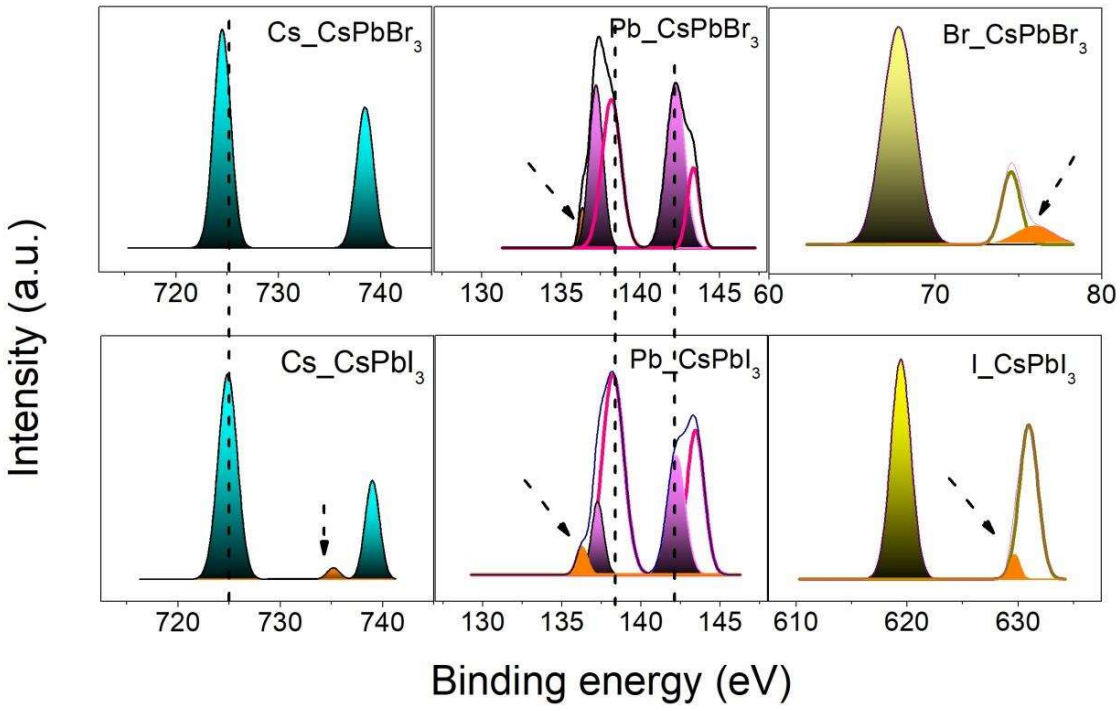

Figure 4.7: De-convoluted elemental XPS spectrum along with the spin orbit interaction for $CsPbBr_3$ and $CsPbI_3$.

4.3.6 Band gap using UV Visible

The optical spectrum is obtained in the wavelength region between 250 nm to 700 nm. In optical absorption spectrum (Fig. 4.8(a)), a strong absorbance edge at 555 nm is observed for $CsPbBr_3$. But $CsPbI_3$ sample shows two absorbance edges at 501 nm and 543 nm. It shows that the absorbance edge in $CsPbBr_3$ is shifted towards higher wavelength than that of $CsPbI_3$. To obtain the value of the band gap energy of studied samples, variation of $(\alpha h\nu)^2$ versus $h\nu$ is plotted (Fig. 4.8(b)). It is observed that for $CsPbI_3$, there are two band gaps while there is only

one band gap in $CsPbBr_3$. The optical band gap energy (E_g) for these materials is estimated from the intercept with the energy axis and is found to be 2.26 eV for $CsPbBr_3$. In case of $CsPbI_3$, band gaps are observed nearly at 2.33 eV and 2.63 eV. This band gap energy change may be attributed to large ionic radii of I^- in comparison to the radii of Br^- [154].

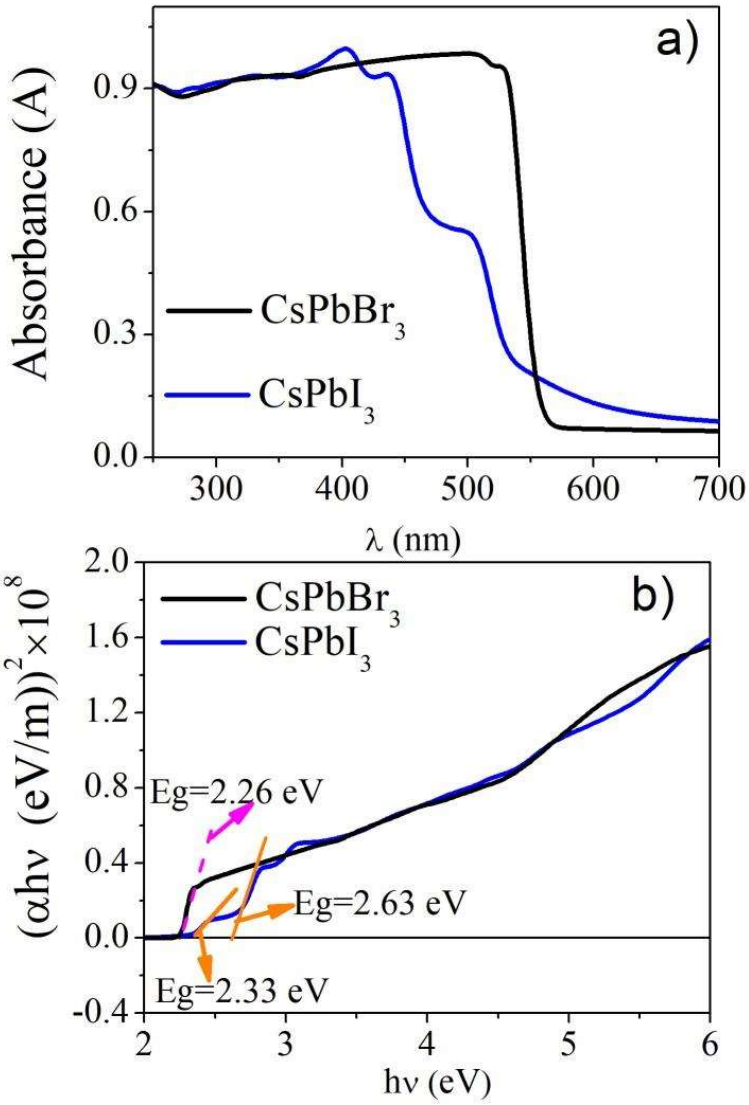

Figure 4.8: Optical absorption spectra for $CsPbBr_3$ and $CsPbI_3$, a strong absorbance edge at 555 nm is observed for $CsPbBr_3$ while, on the other hand, for $CsPbI_3$ two absorbance edges at 501 nm and 543 nm are observed, (b) direct band gap energy estimation from Tauc relation for $CsPbBr_3$ and $CsPbI_3$, respectively.

To evaluate the type of band gap, power factor has been evaluated using the well-known relation [155] (Fig. 4.9).

$$(\alpha h\nu) = A\,(h\nu - E_g)^n \tag{4.2}$$

where α is the absorption coefficient, A is an energy independent constant, E_g is the optical band gap energy, $h\nu$ is the incident photon energy and another constant (n) represents the power factor of transition modes. Taking logarithm on both sides of the equation (4.3) and equation becomes

$$\ln(\alpha h\nu) = n \ln(h\nu - E_g) + \ln A \tag{4.3}$$

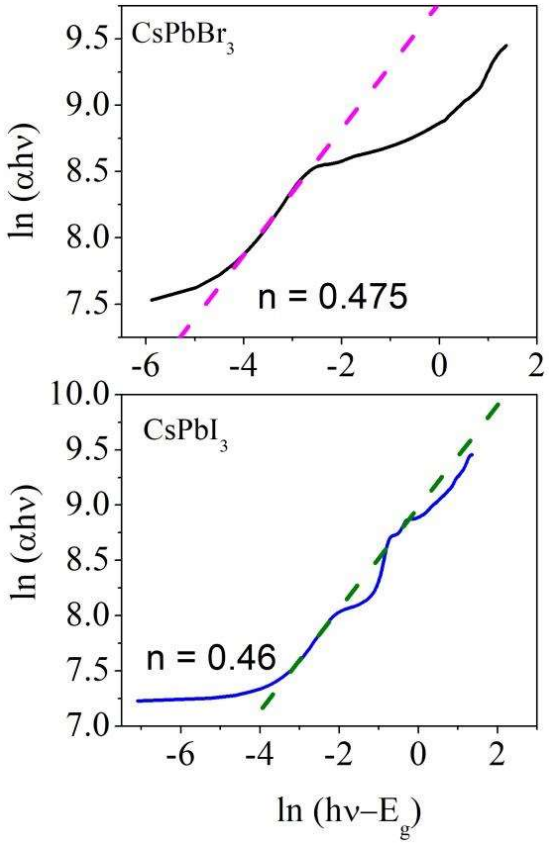

Figure 4.9: Direct allowed transitions in $CsPbBr_3$ and $CsPbI_3$.

Then, comparing the equation (4.3) from the straight line equation y = mx + c. We have obtained the value of slope (m = n), which give the transition modes. To confirm the power factor (n) for direct allowed (n = 1/2), indirect allowed (n = 2), direct forbidden (n = 3/2) and indirect forbidden (n = 3) transitions [156], we have taken the plot of ln ($\alpha h\nu$) versus ln ($h\nu$-E_g). After analyzing the linear curves fitting, we found the values of n. As seen from Fig. 4.9, $CsPbBr_3$ and $CsPbI_3$ possess the direct allowed transitions as the value of power factor (n) are 0.475 and 0.46, respectively (i.e. close to 0.5).

4.3.7 Urbach Energy

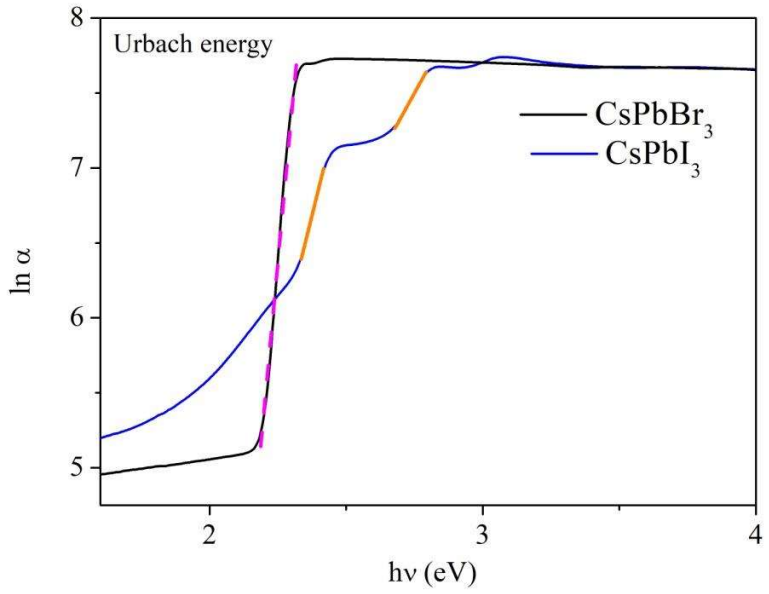

Figure 4.10: Plot of ln (α) versus $h\nu$ (eV) for Urbach energy.

In optical absorption spectra, near band edges have an exponential part called exponential tail (Urbach tail). In the energy range E< E_g, an exponential dependence of the absorption coefficient (α) on photon energy (hν) (Urbach tail) is expressed as [157]:

$$\alpha = \alpha_0 \exp(h\nu/E_u) \quad (4.4)$$

where α_o is a constant and E_u represent the Urbach energy or indicates the energy of the band tail. Taking logarithm both sides of the above equation (4.4)-

$$\ln \alpha = (h\nu/E_u) + \ln \alpha_o \quad (4.5)$$

Here, Urbach energy is the inverse of the slope of equation 4.5. Figure 4.10 shows the plot of ln (α) versus $h\nu$ (eV) for Urbach energy estimation. The value of E_u obtained from the slope (m) of linear fit analysis of these curves for $CsPbBr_3$ is 50 meV and in case of $CsPbI_3$, the values of the Urbach Energy obtained are 135 meV and 303 meV corresponding to the band gaps 2.33 eV and 2.63 eV, respectively. The Urbach energy for $CsPbI_3$ is higher than that of $CsPbBr_3$. It is attributed to the perturbation of structural disorder in $CsPbI_3$ and is in correlation with the strain obtained from structure [148].

4.3.8 Structure- optical correlation

It is well known that quantum size of material and defect present in the sample are correlated to optical band gap energy. It is observed that $CsPbBr_3$ is having small unit cell volume, but large crystallite and grain sizes. Also, the lattice of $CsPbI_3$ ($\in$ = 0.09) is more strained than that of $CsPbBr_3$ ($\in$ = 0.03). The Urbach energy and band gap energy are higher for $CsPbI_3$ than $CsPbBr_3$. The lattice orientation of $CsPbBr_3$ is about b-axis but for $CsPbI_3$, it is more about the c-axis. While, $CsPbI_3$ is smallest along b –axis. So, the optical band gap energy is in correlation with the microstructure of materials. The strained matrix generates structural disorder, hence should possess localised states and higher Urbach energy. The strained matrix in $CsPbI_3$ is attributed to the increase in number of stretching modes in comparison to $CsPbBr_3$. To further verify the structural disorder observed in Urbach energy, we have coupled it with the FWHM of the Raman mode at ~ 110 cm^{-1} which is lower in $CsPbI_3$

(19.70 cm^{-1}) than $CsPbBr_3$ (33.42 cm^{-1}). This decrease in FWHM increases the structural disorder and hence, Urbach energy. The shifting of the peak at ~ 110 cm^{-1} of $CsPbI_3$ increases the strain and hence the band gap has increased in $CsPbI_3$.

4.3.9 Thermo-optical correlation

The enthalpy obtained from thermodynamics is correlated with band gap through the empirical relation [158], [159],$E_g = A\exp(0.34 \times E_{\Delta H^\circ})$ where A is a pre exponential factor, a property of the cation and as reported earlier, value of A is 1.35 for p-block elements, E_g is the band gap and $E_{\Delta H^\circ}$ is the energy obtained from enthalpy using following relation

$$E_{\Delta H^\circ} = -5.22 \times 10^{19}\left(\frac{\Delta H_f^\circ}{Nne}\right)$$

Where ΔH_f° (in cal/mol) is the standard enthalpy of the formation of halides, N is Avogadro's number and ne is the number of electrons transferred in the reaction. $E_{\Delta H^\circ}$ correspond to the energy levels related to one metal-halide bond in the halide. These relations are used in oxides and found true for halides as well in the present case. In the present case, the ratio of band gap obtained thermodynamically using enthalpy is $\left(\frac{E_{g,Br}}{E_{g,I}} = \frac{\exp(0.34\times E_{\Delta H^\circ})_{Br}}{\exp(0.34\times E_{\Delta H^\circ})_I} =\right)$ 1.03 the ratio of band gap obtained from UV-visible data is 0.96.

4.3.10 Stability

The thermodynamics of the $CsPbI_3$ and $CsPbBr_3$ ssynthesized by Cold Sintering method, suggest these compounds are stable. The structure of these materials has been re-examined time to time. The comparative between normalized XRD patterns and UV spectra for 0 day

(i.e., freshly prepared sample) and after, 100 days (i.e., aged sample)) are plotted for the two samples and shown in Fig 4.11. It is observed that there is no difference in the XRD peak positions for $CsPbBr_3$ (Fig. 4.11(a)) whereas, for $CsPbI_3$ (Fig. 4.11(b)) the peak positions are slightly shifted towards higher angle. However, the UV absorption spectra in the both cases (Fig. 4.11(c-d)) show very small increase in the band-gap. Thus, the samples prepared by the cold sintering methods are well stable in structure and absorption spectra with time (for more than 100 days).

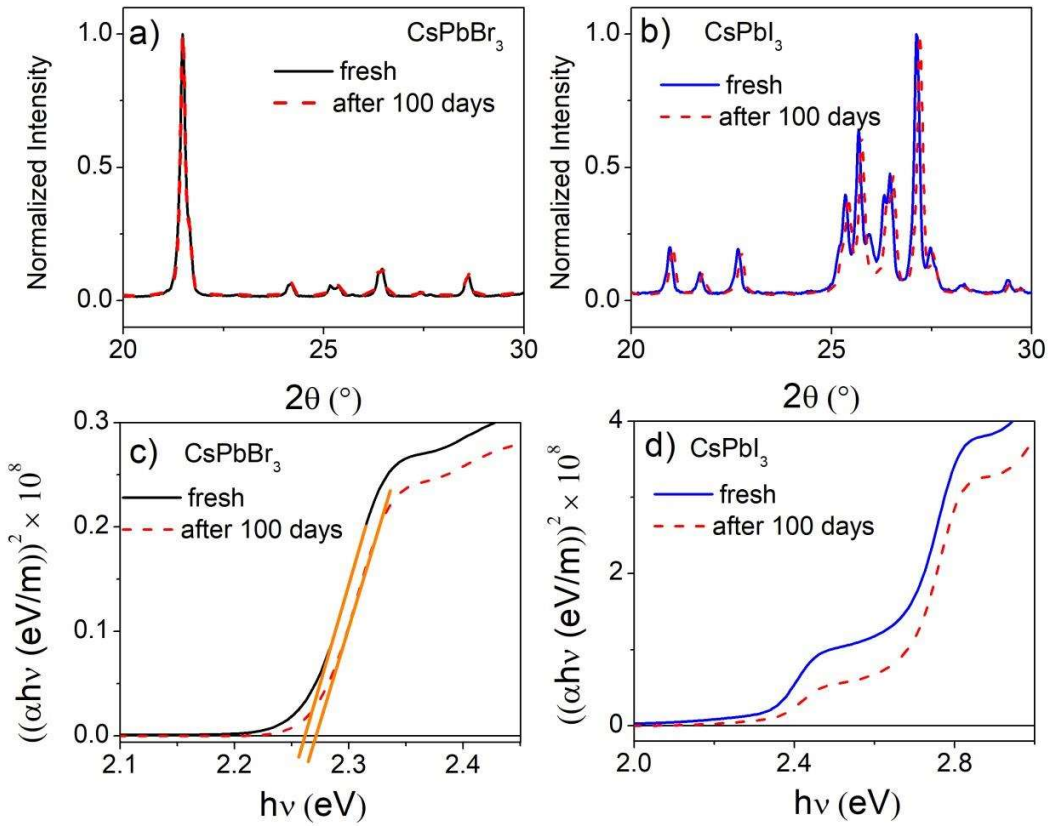

Figure 4.11: The comparative normalized XRD patterns in case of (a) $CsPbBr_3$, (b) $CsPbI_3$. The comparative UV absorption spectra in case of (c) $CsPbBr_3$, (b) $CsPbI_3$. (between 0 day (i.e., freshly prepared sample) and after, 100 days (i.e., aged sample)).

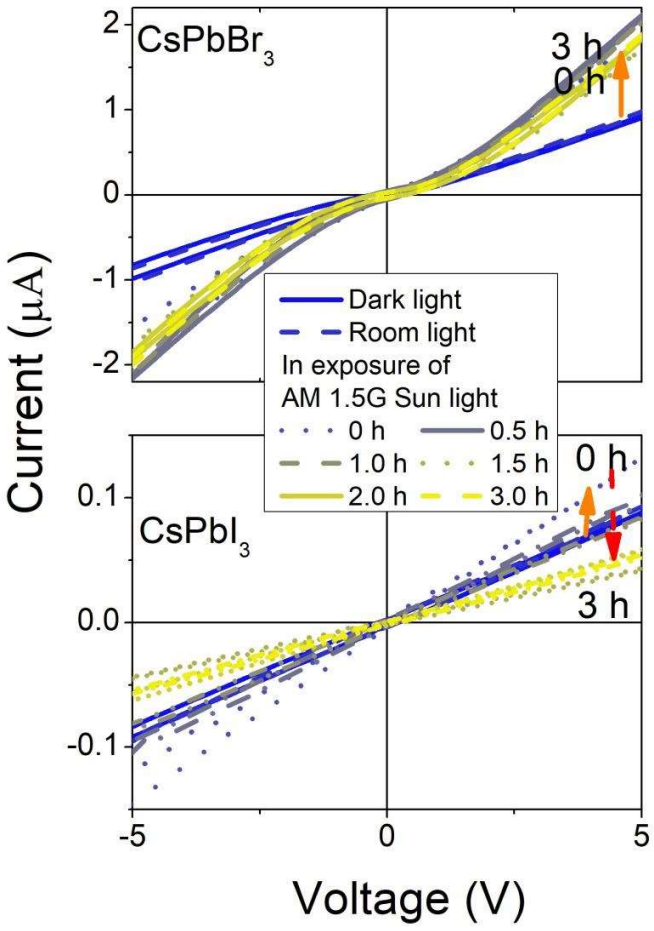

Figure 4.12: Current (I) -Voltage (V) plot in different light exposure (Dark, room light and AM 1.5 G Sun light) along with current degradation with time (0 h -3.0 h) in AM 1.5 G Sun light.

Further, to see the stability of the samples in Sun light exposure, the I-V curves are recorded in the interval of the 30 minutes over the duration of 3 h in the continuous exposure of AM 1.5G Sun light (Fig. 4.12). For both the samples, the current response is observed as soon as AM 1.5G Sun light switched on, as compared from the dark light and room light. However with the time, no significant degradation is observed for $CsPbBr_3$ but for $CsPbI_3$, the degradation in the AM 1.5G Sun light was significant as evident from I-V plot for these two samples.

4.3.11 Comparative (on the basis of synthesis techniques) of structural and optical properties.

The comparative table (Table 4.2) of band gap energy observed for these two samples synthesized with other significant methods indicates that the value is smallest for the samples prepared by cold sintering. In addition, $CsPbBr_3$ synthesized through cold sintering is more stable than $CsPbI_3$ prepared by the same method on exposure to AM 1.5G sunlight.

Table 4.2 Comparative (on the basis of synthesis techniques) of structural and optical properties

Materials	Synthesis method	Band gap (eV)		Ref.
		$CsPbBr_3$	$CsPbI_3$	
$CsPbBr_3$ and $CsPbI_3$	Solution phase synthesis (Nanowires)	2.38	2.71	[160]
$CsPbBr_3$	Transformation doping method (Nanocrystals)	2.84	x	[161]
$CsPbBr_3$	Quantum dot	2.39	x	[162]
$CsPbI_3$	One-pot solution spin coating	2.82	x	[163]
$CsPbBr_3$	Facile synthesis	2.35	x	[164]
$CsPbBr_3$	2-step sequential deposition technique	2.36	x	[165]
$CsPbBr_3$ and $CsPbI_3$	Spin coating	2.3	2.82	[166]
$CsPbI_3$	Thin film by Thermal Evaporation	x	3.013	[167]
$CsPbBr_3$	two step-sequential deposition	2.39	x	[168]
$CsPbBr_3$ and $CsPbI_3$	Cold Sintering	2.26	2.33	In present work

x- Not reported

Non-Linear Conduction Mechanism in Perovskite Halide $CsPbI_3$

In the previous section, the $CsPbI_3$ sample was successfully synthesized by the cold sintering method via the solid-state reaction (SSR) route. In this part, the hopping conduction, and relaxation mechanisms are studied with temperature. For this, electrical properties are characterized by the real and imaginary part of the permittivity, modulus, and ac conductivity within the frequency range 10 to 10^6 Hz for different temperatures between room temperature to 153 °C. The AC conductivity spectra are fitted by Jonscher's power law(JPL) to find the species and motion of species. The activation energy was estimated from the relaxation frequency (f_{max}) obtained from the Modulus Nyquist plots and the dc conductivity obtained from JPL using the Arrhenius relation.

4.4 Results and Discussion

4.4.1 Electrical Characterization (AC Conductivity Studies)

The conductivity spectrum contains two parts: a constant region as plateau and dispersion regions at lower and higher frequency, respectively. The frequency dispersion conductivity curves are studied from RT to 153 ^oC and Figure 4.13(a) shows the variation of log σ vs log ν (conductivity isotherms) at 84 ^oC, 114^oC, 133^oC, and 153^oC for $CsPbI_3$. Normally, the conductivity isotherms comprise a plateau in the lower frequencies range and a sharp rise at higher frequencies. However, in the present case, the low-frequency region (plateau region) is scattered while the high-frequency region is proportional to frequency. The plateau here observed is scattered suggests the incomplete hopping of charge carriers whereas high frequency is showing dispersion with frequency (as reported unsuccessful hopping)

[169],[170]. To identify the species and motion of species, the conductivity isotherms are fitted with the Jonscher power law(JPL) [171],[172].

$$\sigma'(\upsilon) = \sigma(0) + A\upsilon^n \tag{4.6}$$

Where $\sigma(0)$ represents the zero-frequency limit of $\sigma'(\upsilon)$. n is a frequency exponent and A indicates the pre-exponential factor which is the function of temperature and composition. Equation 4.6 can be written as

$$\sigma'(\upsilon) = \sigma(0)\left[1 + \frac{A\upsilon^n}{\sigma(0)}\right]$$

$$\sigma'(\upsilon) = \sigma(0)\left[1 + \left(\frac{\upsilon^n}{\upsilon_H^n}\right)\right] \tag{4.7}$$

Where $\upsilon_H = \left(\frac{\sigma(0)}{A}\right)^{1/n}$ Equation 4.7 is known as Almond and West formulation of Jonscher power law.

It is observed that there are two regimes (shown a vertical line) from 10 to 10^4 Hz and 10^4 Hz to 10^6 Hz showing the grain and grain boundary contributions. Further, the grain boundary is not showing the hopping of charge carriers. The dc conductivity obtained from the plateau region (at a low frequency of the conductivity spectrum. Figure 4.14 shows the Arrhenius plots (σ_{dc} (T) = σ_0 exp[−E_a/ kT]) using dc conductivity extracted from JPL for the two regimes.

σ_{dc} (T) = σ_0 exp$\left[-\frac{E_a}{KT}\right]$ (Taking log both sides)

$$\log \sigma_{dc}(T) = \log \sigma_0 - \frac{E_a}{KT}$$

$$\log \sigma_{dc}(T) = \log \sigma_0 - \frac{E_a}{K\times 1000}\times\frac{1000}{T}$$

Then, comparing the above equation from the straight line equation y = mx + c. We have obtained the value of slope ($m = \frac{E_a}{K \times 1000}$). Where, σ_0, E_a, K, and T are the pre-exponential factor, activation energy, Boltzmann constant, and absolute temperature, respectively. A linear fit of σ_{dc} vs 1000/T plot has been used to evaluate the activation energies. Thus activation energy values were obtained (by linear fitting of the Arrhenius plot) for grain and grain boundary.

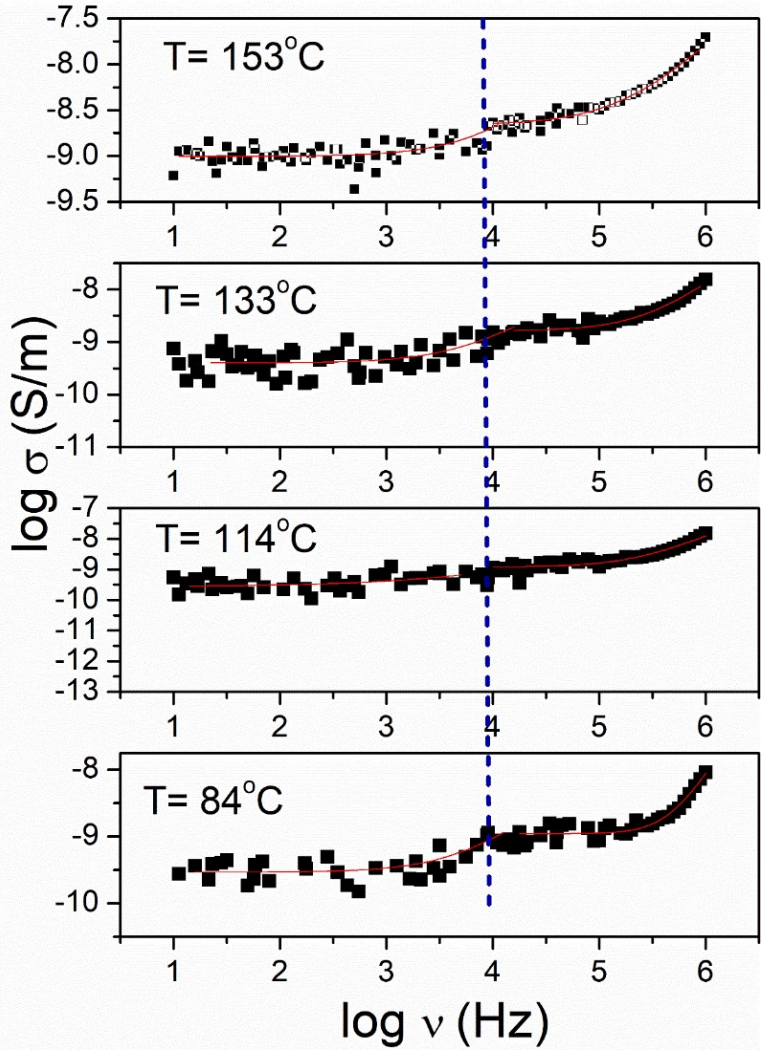

Figure 4.13: Variation of log σ with log ν at 84 °C, 114°C, 133°C and 155°C for $CsPbI_3$. The red lines are fitted lines using JPL with goodness fits ($\langle r^2 \rangle \geq 0.96$).

It is observed that before transition (at 133 ^{o}C) there are slopes, found to be 0.228 eV for grain and 0.41 eV for grain boundary while after transition, activation energy is 0.098 eV suggesting the I_i formation (I interstitial) [173],[174].

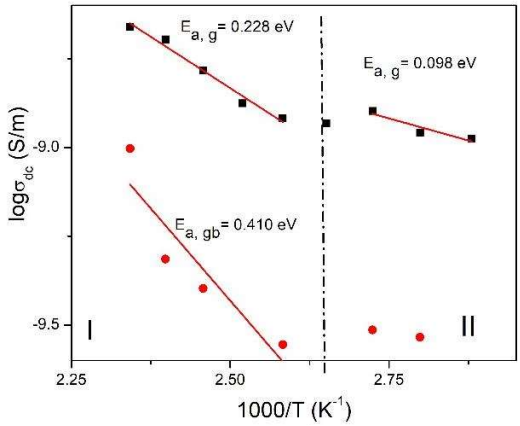

Figure 4.14: Arrhenius plots using dc conductivity with temperature for grain and grain-boundary and goodness fits ($\langle r^2 \rangle \geq 0.98$).

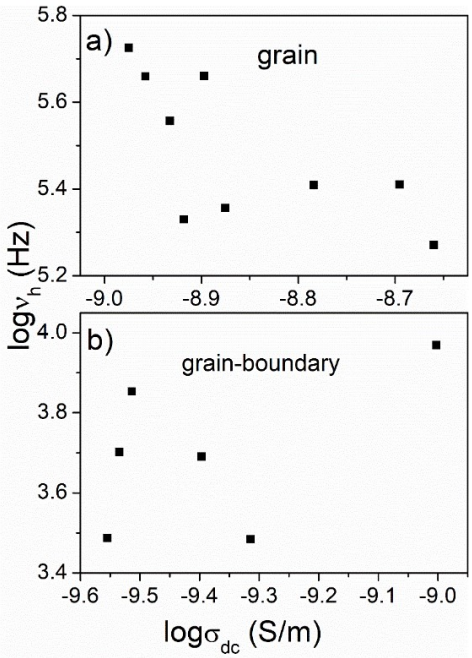

Figure 4.15: (a) Variation of log σ_{dc} with log ν_h for grain (b) Variation of log σ_{dc} with log ν_h for grain- boundary.

To verify the hopping mechanism of charge carriers, the parameters σ_{dc} and ν_h are plotted for grain and grain boundary respectively (Figure 4.15 (a and b). If the slope is linear then the conduction is mainly hopping governed. The data observed is scattered for grain as well as a grain boundary. However, for grain, transition at 133 ^oC shows two slopes that differ from unity. This is observed following the exponent observed from JP law fitting of conductivity isotherms. The variation of exponent (grain) with temperature (Figure 4.16) is observed to decrease with temperature and the value is greater than unity showing super linear behavior which is observed due to the hopping between different potential barriers corresponding to different defect centers and heights correlated with columbic interaction [175]. This coulombic interaction is leading to the different hopping distances and incomplete hopping of charge carriers in the grain and grain – boundary.

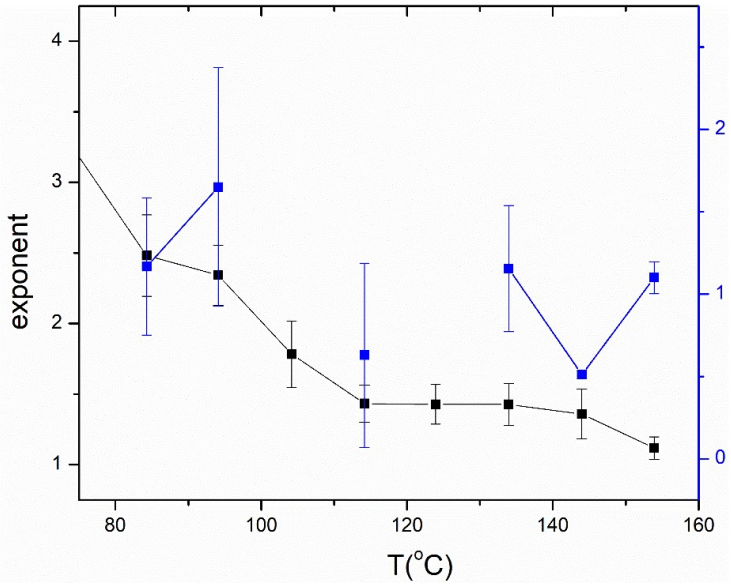

Figure 4.16: Variation of exponent with temperature for grain and grain-boundary.

It is observed that a change in slope in Figure 4.14, this discontinuity can occur may be the phase transition temperature. Further, this slope change leads to the change in the activation

energy from 0.228 eV to 0.098eV for grain and in the case of grain-boundary, E_a is 0.41eV. This shows the creation of V_I vacancies and with temperature movement of I to I_i [55].

4.4.2 Relative Permittivity Analysis

To identify the phase transition temperature, ε' and ε" (real and imaginary parts of permittivity, respectively) are plotted with the temperature at 10 kHz, 100 kHz, and 1MHz frequencies (Figure 4.17). Permittivity is a complex quantity can be expressed as $\varepsilon^*(\omega) = \varepsilon'(\omega) - j\varepsilon''(\omega)$, where, real part $\varepsilon'(\omega)$ and imaginary part $\varepsilon''(\omega)$ of the permittivity represents the charge storing capability and entire energy loss within the materials. The real and imaginary parts of the permittivity have been estimated by using the euation (4.8) and (4.9).

$$\varepsilon'(\omega) = \frac{Z''}{\omega C_o(Z'^2+Z''^2)} \tag{4.8}$$

$$\varepsilon''(\omega) = \frac{Z'}{\omega C_o(Z'^2+Z''^2)} \tag{4.9}$$

Where $\omega=2\pi f$ and $C_o = \varepsilon_o A/t$ (A is cross sectional area and t is the thickness of the pellet, and ε_o is the free space permittivity). It is observed that ε' and ε" are constant up to 380 K and then a kink is observed followed by another plateau (gray region). This kink is following the change in slope observed in activation energy plots.

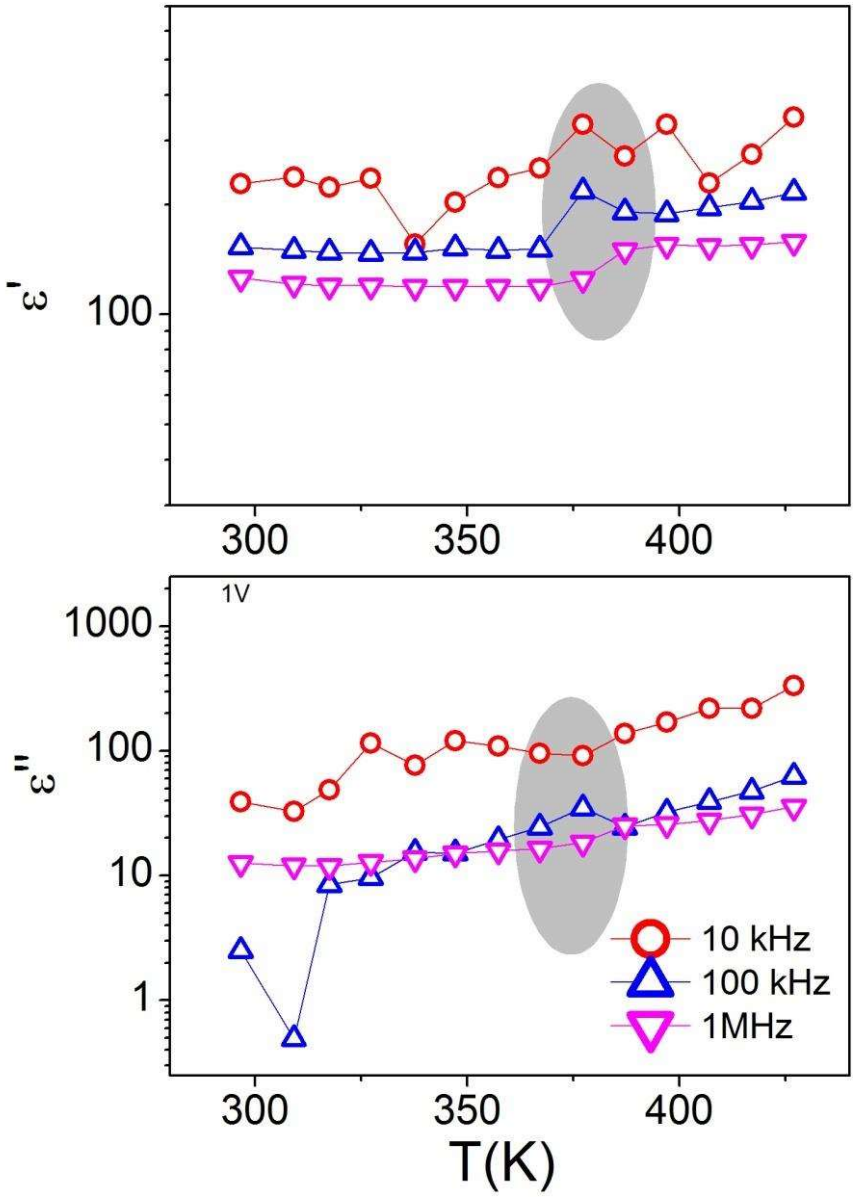

Figure 4.17: Variation of ε' and ε'' (real and imaginary parts of permittivity, respectively) are plotted with the temperature at 10 kHz, 100 kHz, and 1MHz frequencies.

4.4.3 Electrical Modulus

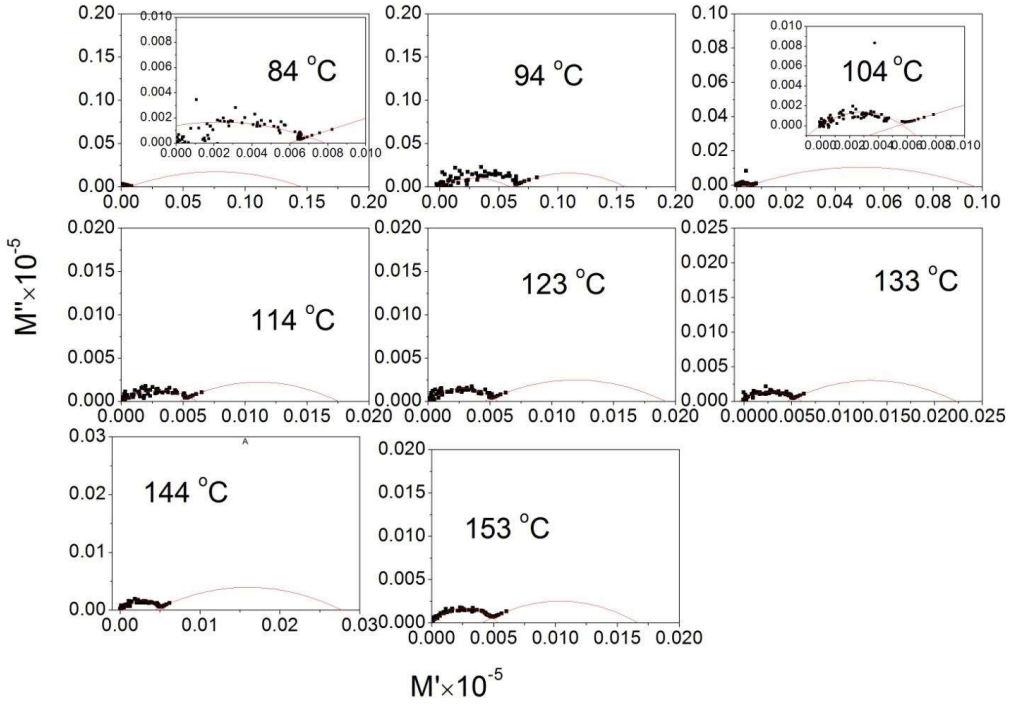

Figure 4.18: Shows the fitting of the Modulus Nyquist plots over the temperature range from 84 °C to 153 °C and goodness fits ($\langle r^2 \rangle \geq 0.96$).

To confirm two contributions in ac conductivity isotherms we have studied the modulus Nyquist plots. The electrical modulus is a complex quantity $M^*(\omega) = M'(\omega) + jM''(\omega)$ and inverse of the relative permittivity ($M^*(\omega) = \frac{1}{\varepsilon^*(\omega)}$). Fig. 4.15(a) shows the Modulus Nyquist plot at 153 °C and it can be seen that there are two contributions (through a depressed semi-circular arc and a spike). Being a Modulus spectra, this rules out the possibility of electrode effect, thus two contributions correspond to the grain and grain-boundary. Further, the activation energy has been estimated from the relaxation frequency (f_{max}) obtained from the Modulus Nyquist plots. The relaxation time, τ, observed is in the range of 10^{-4} to 10^{-5} sec. Fig. 4.19(b) depicts the Arrhenius plots for activation energy (variation of $\ln(\tau)$ vs 1000/T) and observed that E_a = 0.534 eV and 0.801 eV in the two regimes before and after the transition.

In the Pb- poor conditions, firstly, V_{Pb} vacancies are created (0.801eV) at low temperature and then V_I vacancies are created (0.534 eV) at high temperature [176].

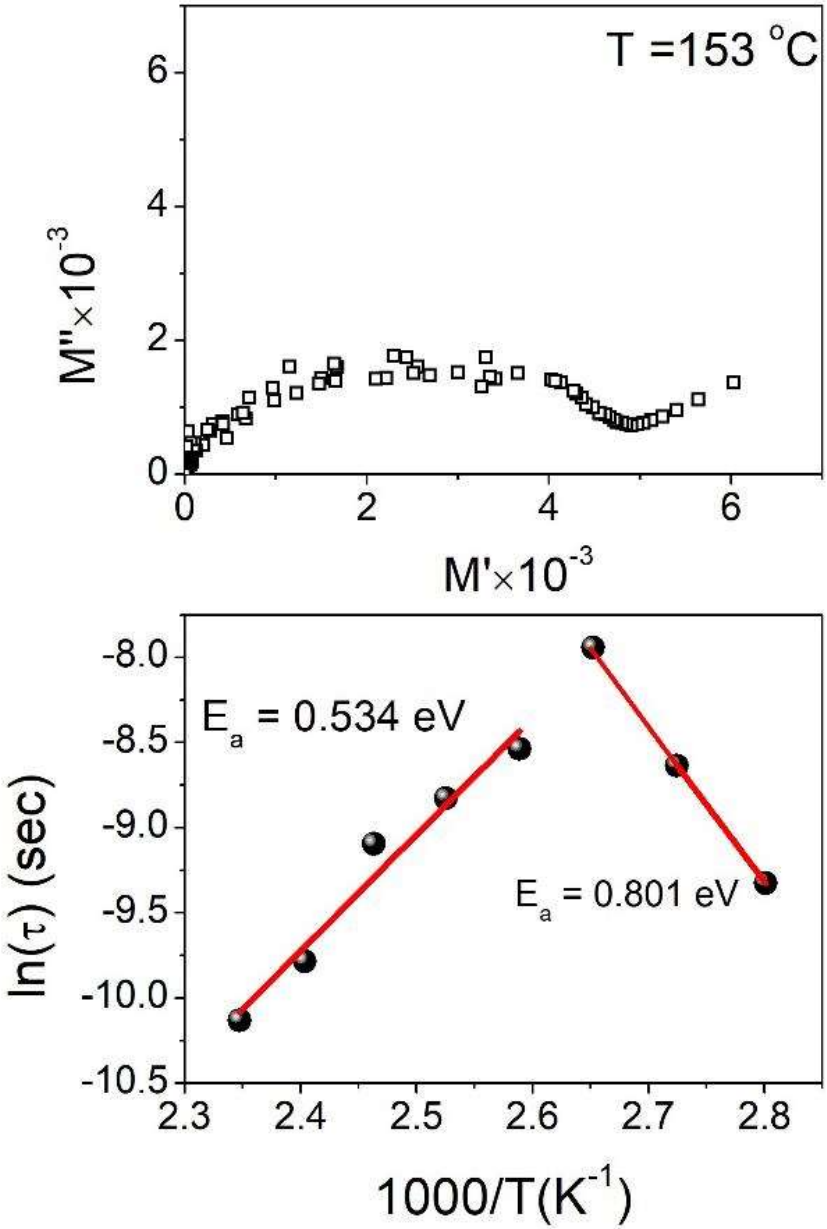

Figure 4.19: (a) Shows the Modulus Nyquist plot at 153 °C and (b) Arrhenius plots showing the variation of ln(τ) vs 1000/T and goodness fits ($\langle r^2 \rangle \geq 0.98$).

.

It can be noticed from Fig. 4.14 that the activation energy for grain is lower than grain boundary which can be due to the increased scattering of charge carriers which are present at the grain –boundaries leading to the disorder. Further, we have observed that in the low temperature regime, the activation energy observed from conductivity measurement is different from the relaxation mechanism. There are number of processes occurring simultaneously at a time which depend on temperature, composition and frequency. In these materials, point defects are created, V_{Pb}'', $V_I^{\bullet}$ and I_i with temperature over conduction and relaxation. These form dipoles (orientable or re-orientable) and at low temperature these processes leads to localized conduction and orientation polarization. Further, at low temperature, thermal conduction only participates leading to the different activation energies obtained from conductivity and relaxation mechanism.

To illustrate the polarization (relaxation) mechanism, bode plots of permittivity (ε) are plotted with temperature. We further fitted the complex permittivity using various relaxation distribution models (Debye, Cole-Cole(CC) and Cole- Davidson (CD)) along with general Havriliak-Negami (HN) model and found that the permittivity curves are best fitted with Cole-Davidson method.

$$\frac{\varepsilon^* - \varepsilon_{op}}{\varepsilon_s - \varepsilon_{op}} = \frac{\varepsilon^* - \varepsilon_{op}}{\Delta\varepsilon} = (1 + (i\omega\tau)^{1-\alpha})^{\beta-1} \quad (4.10)$$

Where, α and β are the symmetric and asymmetric (loss peak) exponent parameters. τ, ε_{op}, ε_s are the relexation time, high frequency permittivity and low frequency permittivity, respectively

Figure 4.20 shows bode plots of permittivity with temperature and their fitting with Cole-Davidson model. We observed the relaxation time of the order 10^{-4}-10^{-6} sec suggesting the migration of I^- ions at the interstitial sites or its antisites as confirmed earlier.The fitting achieved through Cole-Davidson model suggest the formation of dipoles at the interface with the excusion of space charge polarization.

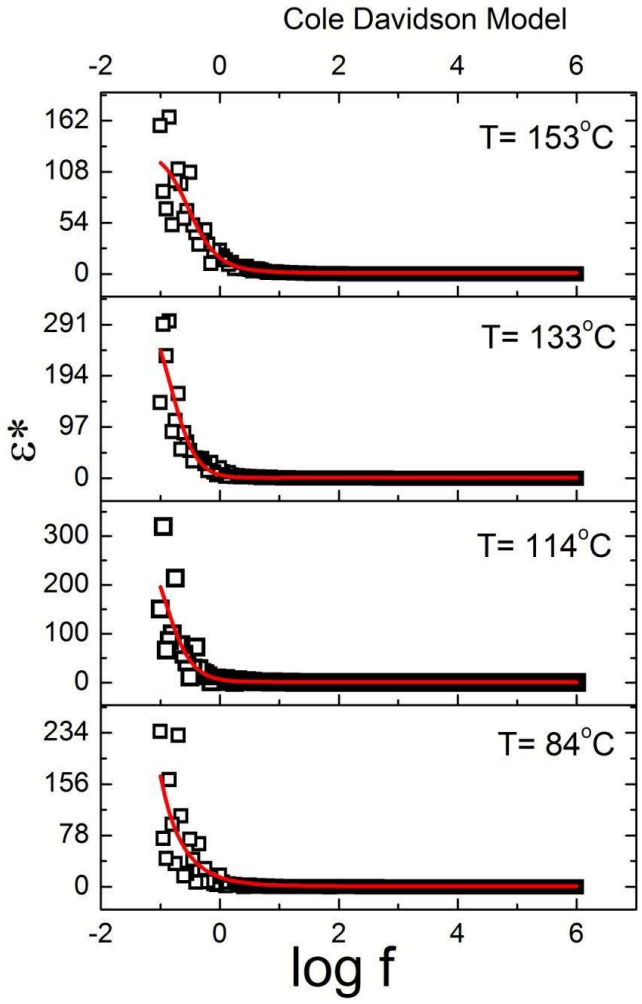

Figure 4.20: Bode plots of permittivity (ε) with temperature and fitting with Cole- Davidson equation and goodness fits ($\langle r^2 \rangle \geq 0.98$).

4.5 Conclusion

Synthesis and stability are major concerns for these materials. The major work on these materials has been done in inert atmosphere, which is just against the primary criterion of cost effective solar cell materials. The synthesis of halide perovskite thin film is still difficult despite the availability of many synthesis techniques. But, contrary to it, in our very first attempt it is found that sample can be synthesized in the ambient environment through SSR technique and hence low cost synthesis as compared to the other reported synthesis methods in inert atmosphere has been achieved. Further, the synthesized material can withstand with duration over the changing environment. Hence, it's not intrinsic instability which governs the formation. The samples synthesized through cold sintering method are favored thermodynamically as there entropy is constant. The band gap energy observed for these two samples synthesized with other significant methods indicates that the value is smallest for the samples prepared by cold sintering. Moreover, $CsPbBr_3$ is more stable than $CsPbI_3$ on exposure to AM 1.5G sunlight.

Cesium lead iodide material was synthesized by cold sintering method via solid-state reaction (SSR) route. The relaxation time, τ, observed is in the range of 10^{-4} to 10^{-5} sec suggesting the migration of I^- ions at the interstitial sites or its antisites. In the Pb- poor conditions, firstly, V_{Pb} vacancies are created (0.801eV) at low temperature and then V_I vacancies are created (0.534 eV) at high temperature. It is concluded that the activation energy for grain is lower than the grain boundary which indicates to increase in the scattering of charge carriers that are present at the grain boundary. Further, in the low-temperature regime, the activation energy observed from conductivity measurement is different from the relaxation

mechanism. Thus, the formation of point defects leads to different conduction and relaxation mechanisms. The fitting achieved through Cole-Davidson model suggest the formation of dipoles at the interface with the excusion of space charge polarization.